

On-Stack Two-Dimensional Conversion of MoS₂ into MoO₃

Taeg Yeoung Ko,¹ Areum Jeong,¹ Wontaek Kim,² Jin Hwan Lee,³ Youngchan Kim,³ Jung Eun Lee,¹ Gyeong Hee Ryu,⁴ Zonghoon Lee,⁴ Min Hyung Lee,¹ Changgu Lee³ and Sunmin Ryu^{2,5*}

¹Department of Applied Chemistry, Kyung Hee University, Yongin, Gyeonggi 446-701, Korea

²Department of Chemistry, Pohang University of Science and Technology (POSTECH), Pohang, Gyeongbuk 790-784, Korea

³School of Mechanical Engineering, Sungkyunkwan University, Suwon, Gyeonggi 440-746, Korea

⁴School of Materials Science and Engineering, Ulsan National Institute of Science and Technology (UNIST), Ulsan, 689-798, Korea

⁵Division of Advanced Materials Science, Pohang University of Science and Technology (POSTECH), 50 Jigokro-127, Pohang, Gyeongbuk 790-784, Korea

*E-mail: sunryu@postech.ac.kr

Abstract

Chemical transformation of existing two-dimensional (2D) materials can be crucial in further expanding the 2D crystal palette required to realize various functional heterostructures. In this work, we demonstrate a 2D “on-stack” chemical conversion of single-layer crystalline MoS₂ into MoO₃ with a precise layer control that enables truly 2D MoO₃ and MoO₃/MoS₂ heterostructures. To minimize perturbation on their 2D morphology, a nonthermal oxidation using O₂ plasma was employed. To the early stage of the reaction was characterized by the defect-induced Raman peak, drastic quenching of photoluminescence (PL) signals and sub-nm protrusions in atomic force microscopy images. As the reaction proceeded from the uppermost layer to buried layers, PL and optical second harmonic generation signals showed characteristic modulations revealing a layer-by-layer conversion. The plasma-generated 2D oxides, confirmed as MoO₃ by X-ray photoelectron spectroscopy, were found to be amorphous but extremely flat with a surface roughness of 0.18 nm, comparable to that of 1L MoS₂. The rate of oxidation quantified with Raman spectroscopy decreased very rapidly for buried sulfide layers due to protection by the surface 2D oxides, exhibiting a pseudo-self-limiting behavior. As exemplified in this work, various on-stack chemical transformations can be applied to other 2D materials in forming otherwise unobtainable materials and complex heterostructures, thus expanding the palette of 2D materials building blocks.

Keywords: MoS₂, MoO₃, plasma oxidation, Raman spectroscopy, photoluminescence, optical second-harmonic generation

Since the first mechanical exfoliation of 2-dimensional (2D) crystalline graphene,[1, 2] various dielectric and semiconducting analogues represented by h-BN and MoS₂ have been isolated revealing many of new scientific phenomena and principles.[3-9] Despite being incompatible with mass production of large area samples, this simple method can be applied to essentially any layered materials with weak interlayer interaction,[3] still remaining as one of the best methods for high quality crystals.[10, 11] Since most of single layer (1L) transition metal dichalcogenides (MX₂, where M and X denote metal and chalcogen, respectively) were predicted to be thermodynamically stable,[12] the palette of 2-dimensional crystals can be filled with tens of metallic, semiconducting and insulating “colors”. In contrast to the “top-down” exfoliation, it was also shown that 2D crystals and their heterostructures can be constructed “bottom-up” from appropriate building blocks via chemical routes as demonstrated by the vapor deposition of graphene and other crystals.[13-17] Alternatively, arbitrarily stacked extended 2D structures can be formed by physically stacking one 2D crystal on top of another exploiting interplanar van der Waals (vdW) interactions.[18] Even with limited “colors” available, there have already been interesting 2D heterostructure-related reports such as tunable metal-insulator transitions,[19] field effect tunneling transistors,[20] photodetectors,[21] *etc.*

Chemical transformation of existing 2D materials may also be useful in further expanding the 2D crystal palette required to realize various functional heterostructures. The top single, few or even all layers of supported 2D materials may be selectively transformed into another of different chemical nature by choosing appropriate chemical reactions. Such “on-stack transformations” may form 2D materials that are not readily generated via the conventional synthetic routes or physical vdW stacking routes. This presents a challenge and opportunity for chemists and materials scientists to explore and develop various chemical reactions that can be applied to each type of 2D crystals. Considering the high aspect ratio (length-to-thickness) of 2D materials, a precise control over the thickness of modified layers further requires a given reaction to be highly uniform across the basal planes. In addition, chemical reactions of 2D materials are also of fundamental significance and deserve systematic investigation since their unique geometric and electronic properties may lead to novel phenomena and findings characteristic of the low dimensional materials. For example, the chemical reactivity of 1L graphene was shown to be much higher than few layer graphene for facile out-of-plane distortion[22-24] or larger susceptibility towards external charge doping.[25] Even the edges of graphene are distinct from the inner area in terms of chemical reactivity[24] and electronic properties.[26] The presence of solid substrates, atomically rough in most cases, has profound effects on the geometric[10, 11, 27] and electronic structures,[28] chemical reactivity[23] and wettability[29] of the supported graphene.

In this regard, the chemical transformation between chalcogenides of transition metals can be a model reaction

to explore the chemistry of 2D materials. Whereas the disulfides and diselenides of molybdenum have a strong tendency towards oxidation,[30] the resulting trioxides may also be reduced to dichalcogenides in excess of chalcogenic precursors at elevated temperatures.[31, 32] Atomically thin MoS₂ has been well studied drawing a great interest for its direct-indirect bandgap transition[5, 7] depending on the number of layers thus revealing rich photophysics[33] and allowing various optoelectronic applications.[34] MoO₃, with a larger bandgap (>2.7 eV), is photochromic[35] and also electrochromic,[36] and thus has been actively investigated for their potentials in displays and smart windows.[37] With a large work function of 6.7 eV, MoO₃ films also serve as hole dopants as well as hole transport layers.[38] Due to its high dielectric constant, MoO₃ may serve as an ideal gate dielectric[38] for atomically thin transistors based on 2D semiconductors.[39] Although there have been many studies on thin MoO₃ films formed by thermal and sputter deposition,[37] their surfaces exhibited a typical roughness larger than a few nm[40] thus far from the layer-by-layer precision that can be routinely achieved with various 2D crystals. Since atomically thin MoS₂ layers of high crystallinity or large area can be prepared respectively by the exfoliation[3] or CVD method,[41] 2D oxides of atomic thickness may be generated by chemical transformation of the 2D sulfides. In this work, we demonstrate O₂-plasma-based conversion of 2D MoS₂ crystals into highly flat 2D MoO₃ or MoO₃/MoS₂ heterostructures with a layer-by-layer precision. As increasing the plasma oxidation time, the Raman and photoluminescence (PL) intensity from MoS₂ decreased indicating loss of the sulfides. X-ray photoelectron spectroscopy (XPS) showed that Mo⁶⁺ increased at the expense of Mo⁴⁺, confirming the conversion. Optical second-harmonic generation (SHG) spectroscopy revealed a drastic alternation in intensity, which is explained by breakage and recreation of inversion symmetry in the remaining crystalline sulfides. The plasma-generated 2D oxides were highly flat with a typical roughness of 0.18 nm. The thickness of a single layer oxide was 1.8 ± 0.1 nm, ~2.5 times the interlayer spacing of crystalline α-MoO₃. Systematic Raman and atomic force microscopy (AFM) measurements also revealed that the oxidation proceeds from the top layer into the underlying layers with the rate decaying rapidly due to the passivation effect of the surface oxide layers. Our study suggests that similar on-stack chemical transformations can be devised to convert one form of 2D chalcogenide into another or their heterostructures, which should expand the palette of 2D materials.

Results and Discussion

Raman spectroscopic characterization of 2D sulfides and their oxidation: Figures 1a & 1b show optical micrographs of 1L and 2L MoS₂ (1L_{MS} and 2L_{MS}, respectively) obtained before and after a series of exposures to low-frequency O₂ plasma (see Methods for the details). The accumulated exposure time (t_{ox}) represents the total reaction time. The optical contrast of both samples significantly decreased at $t_{ox} \geq 26$ s and the flake of 1L_{MS} could be barely identified for $t_{ox} = 242$ s. The change in the optical contrast was attributed to its conversion to 1L MoO₃

(1L_{MO}) with negligible absorption in the visible range as will be shown below. Similar contrast change was observed for n_{LMS} ($n = 3 \sim 4$) (see Fig. S1). Figure 1c shows the Raman spectra of 1L_{MS} obtained in the ambient conditions for various t_{ox} . Among the four Raman-active modes of bulk 2H-MoS₂ (space group D_{6h}^4),[42] the in-plane E_{2g}^1 and out-of-plane A_{1g} were shown to be useful in determining the number (n) of layers of thin MoS₂ samples.[6] Although their symmetry representations vary depending on n (E' and A_1' for odd-numbered n_{LMS} belonging to D_{3h}^1 space group; E_g and A_{1g} for even-numbered n_{LMS} belonging to D_{3d}^3 space group),[43] the bulk-notations will be used for simplicity according to the original report for 1L.[6] The frequency difference ($\Delta\omega$) of the two Raman peaks was found to be 18.5 cm^{-1} and their widths were comparable to that of the previous report,[6] which confirms that the sample is single-layered. The lack of the defect-activated LA(M) peak also verifies its high structural quality (Fig. S2).[44] As a more direct proof, atomically resolved transmission electron microscope (TEM) images and diffraction patterns were obtained for freestanding 1L samples (Fig. S3).

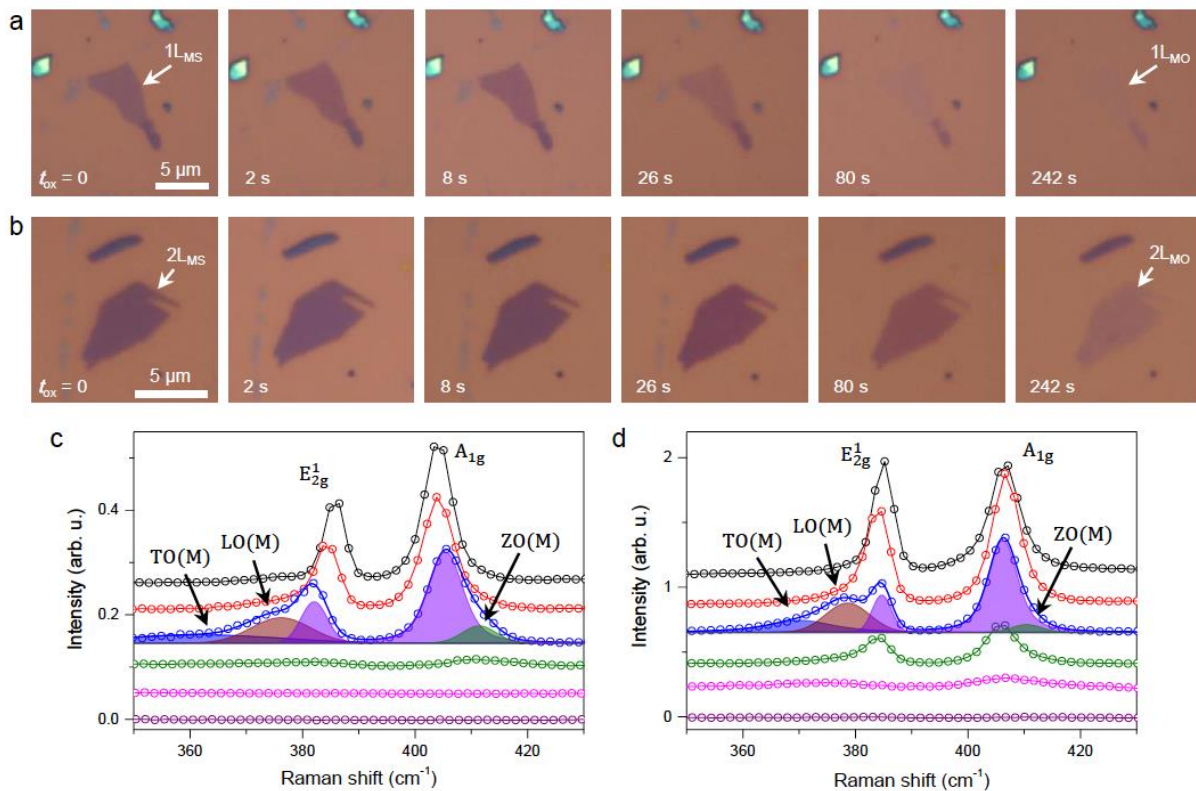


Figure 1. Raman spectroscopic characterization of plasma-oxidized MoS₂. (a) & (b) Optical micrographs of single and double-layer MoS₂ (1L_{MS} & 2L_{MS}) obtained after O₂ plasma for varying oxidation time (t_{ox}). When completely oxidized for 242 s, both samples became transparent indicating formation of corresponding 2D Mo oxides (1L_{MO} & 2L_{MO}). (c) & (d) Raman spectra of 1L and 2L MoS₂, respectively, obtained with increasing t_{ox} (top to bottom): 0, 2, 8, 26, 80 & 242 s. The raw spectra (open circles and solid lines) were offset for clarity. The blue solid lines for $t_{ox} = 8$ s are cumulative fits of five Voigt functions representing the color-shaded Raman peaks: two violets for E_{2g}^1 and A_{1g} , one blue peak for TO(M), one wine for LO(M) and one olive for ZO(M) (see the text for their assignment⁴⁴).

Oxidation induces a few distinctive changes in the Raman spectra. The in-plane Raman mode became softened by $\sim 1 \text{ cm}^{-1}$ on the first exposure for 2 s and downshifted further with the other mode moving in the opposite direction when subjected to additional exposure ($t_{\text{ox}} = 8 \text{ s}$). Since the newly evolving Raman peaks have respectively lower and higher peak frequencies than their pristine counterparts, their frequency difference, $\Delta\omega_{(\text{NC})}$, is $\sim 5 \text{ cm}^{-1}$ larger than that of pristine 1L_{MS} . Both peaks also became broadened asymmetrically and attenuated in intensities. For $t_{\text{ox}} = 26 \text{ s}$ which induced significant loss in the optical contrast in Fig. 1a, for example, the Raman intensities, $I(E_{2g}^1)$ and $I(A_{1g})$ decreased to $\sim 5\%$ of those for the pristine sample with both peaks moving further away from each other and further broadened. The additional exposure ($t_{\text{ox}} = 80 \text{ s}$) lead to no detectible signal for both peaks, indicating complete loss of MoS_2 . Within the phonon confinement model, the oxidation-induced downshift (upshift) of E_{2g}^1 (A_{1g}) can be explained by the relaxation of the fundamental Raman selection rule.[45] In its essence, the defects confining phonons allow scattering of phonons near the zone center with energies lower (higher) than E_{2g}^1 (A_{1g}). The low (high)-frequency shoulders of E_{2g}^1 (A_{1g}) that caused the asymmetric broadening are also due to the defects, which selectively allow scattering of the phonons near the M points in the double-resonance Raman scattering mechanism.[46] Indeed the spectra of partially oxidized 1L and 2L (Fig. 1c & 1d) are well described by the five Voigt functions including the defect-activated TO(M), LO(M) and ZO(M).[44, 45] As discussed in detail below, plasma-generated reactive oxygen species create sub-oxide defects ($\text{MoS}_x\text{O}_{1-x}$) on the basal plane of MoS_2 , essentially forming a nano-crystalline (NC) phase MoS_2 sheet.

The Raman spectra of multi-layered samples showed similar spectral changes also with a layer-by-layer oxidation behavior. The in-plane mode of 2L_{MS} in Fig. 1d, for example, showed a noticeable broadening due to the M-point phonons for $t_{\text{ox}} = 8 \text{ s}$ and became sharper with 40% attenuated intensity for $t_{\text{ox}} = 26 \text{ s}$. An additional exposure ($t_{\text{ox}} = 80 \text{ s}$) lead to further decrease in intensity and significant broadening. The NC-phase observed for $t_{\text{ox}} = 8 \text{ s}$ is formed on the top MoS_2 layer with the bottom layer remained intact. The disappearance of the NC-phase features for $t_{\text{ox}} = 26 \text{ s}$ can be attributed to complete oxidation of the top layer, which is only weakly coupled with the still pristine bottom one responsible for the remaining half of the Raman signals. The second appearance of the broadening for $t_{\text{ox}} = 80 \text{ s}$ indicates that the oxidative attack reached the bottom layer forming NC-phase domains. An additional exposure ($t_{\text{ox}} = 242 \text{ s}$) lead to a complete loss of Raman signal. These observations indicate that the oxidation proceeds in a layer-by-layer manner and is much slow for inner layers that are protected by the outer oxides.

Symmetry characterization by SHG: Since the optical SHG requires the lack of an inversion symmetry,[47] it can serve as a sensitive symmetry probe for chemical modification occurring in thin MoS₂. As shown in Fig. 2a, a strong SHG signal occurred at 400 nm when the fundamental 800-nm Ti:sapphire laser beam with a nominal pulse width of 140 fs was irradiated on non-centrosymmetric pristine 1L_{MS}. [48] An input power dependence of the SHG peak intensity (I_{SHG}) confirmed the two-photon process (Fig. S4). The intensity of the SHG peak (I_{SHG}) indeed decreased by the plasma oxidation and finally reached the zero level for 1L_{MO} ($t_{\text{ox}} = 20$ s), which correlates nicely with the Raman intensity variation of MoS₂ (Fig. 2b). Thus the attenuation of I_{SHG} can be attributed to destruction of 1L MoS₂ crystal. As shown in Fig. 2a, 2L MoS₂ presents a striking contrast to the case of 1L. $I_{\text{SHG}}(2L_{\text{MS}})$ is ~60 times smaller than $I_{\text{SHG}}(1L_{\text{MS}})$ since even-number-layered MoS₂ crystals are centrosymmetric and thus do not support SHG. The residual signal of 2L_{MS} is attributed to a minor interlayer asymmetry induced by the presence of the

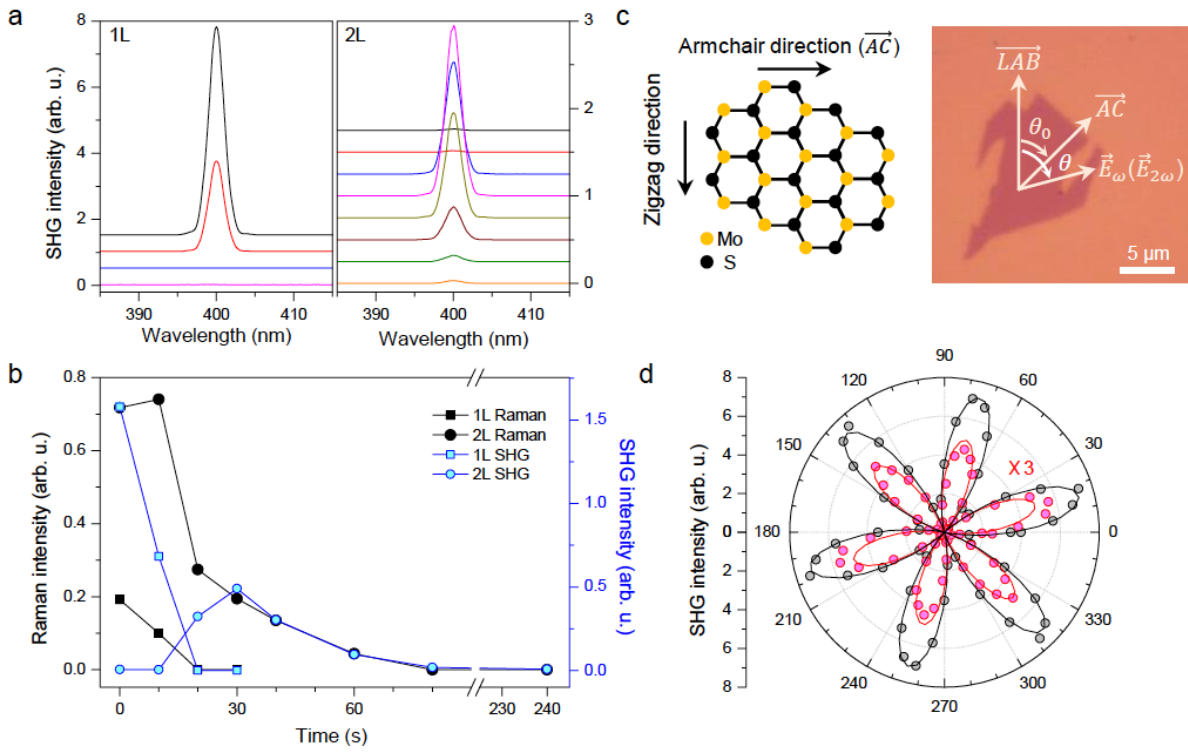


Figure 2. Nonlinear optical characterization of plasma-oxidized MoS₂. (a) Optical SHG spectra of 1L and 2L MoS₂ obtained as increasing t_{ox} (top to bottom): 0, 10, 20, 30, 40, 60, 80 & 240 s. (b) Raman and SHG intensities of 1L and 2L MoS₂ given as a function of t_{ox} . The maximum intensity of 2L for $t_{\text{ox}} = 30$ s amounts to ~1/3 of that for the pristine 1L. (c) Schematic view (left) of MoS₂ lattice with armchair and zigzag edges and an optical image (right) of 1L MoS₂ used in the SHG measurements: With the polarization directions of the input (\vec{E}_ω) and output ($\vec{E}_{2\omega}$) fixed, the sample with a predefined laboratory axis (\overline{LAB}) was rotated by θ . The armchair direction (\overline{AC}) forms an angle (θ_0) with respect to \overline{LAB} . (d) Polar plot of the parallel SHG intensity ($I_{\text{SHG}}^{\parallel}$) of pristine (gray) and half-oxidized (magenta) 1L MoS₂ given as a function of θ . Using the fact that $I_{\text{SHG}}^{\parallel} \propto \cos^2 3(\theta - \theta_0)$ which is represented by the solid lines, the armchair direction of the sample is determined with $\theta_0 = 15.0 \pm 0.2$ degree.

SiO₂/Si substrate.[49] A series of oxidation treatments, however, activated and then deactivated SHG by the 2L flake (Fig. 2a). Figure 2b reveals that I_{SHG} intensity increased at the expense of the Raman signal represented by $I(A_{1g})$. Since I_{SHG} reached its maximum for $t_{\text{ox}} = 30$ s for which the Raman intensity is close to that of 1L_{MS}, the treated sample essentially corresponds to 1L_{MO}/1L_{MS}. This assignment is also supported by the fact that additional treatments lead to a decrease in I_{SHG} indicating oxidative degradation of the bottom sulfide layer. The lack of SHG signal from the completely oxidized layers (1L_{MO} and 2L_{MO}) might be explained if the 2D oxides are a centrosymmetric crystal like bulk α -MoO₃ belong to a space group of D_{2h}^{16} . [50] As will be shown below, however, the 2D oxides are far from α -MoO₃ and more likely to be amorphous and isotropic not generating SHG signal.

Despite the degradation of the crystalline lattice, the crystallographic orientation could still be determined for partially oxidized MoS₂ since I_{SHG} is strongly dependent on the polarization angle $(\theta - \theta_0)$ between the fundamental polarization (\vec{E}_ω) and armchair direction (\vec{AC}) defined in Fig. 2c. For polarization-resolved SHG measurements, samples were rotated to vary θ and the SHG signal parallel to the input polarization, $I_{\text{SHG}}^{\parallel}$, was collected using a polarizer located in front of the detector. The polar plot for 1L_{MS} in Fig. 2d revealed the 6-fold symmetry of $I_{\text{SHG}}^{\parallel} \propto \cos^2 3(\theta - \theta_0)$, [48] which also determined that $\theta_0 = 15.0 \pm 0.2$ degree, the angle of \vec{AC} with respect to a preset laboratory axis (\vec{LAB}). When oxidized to give ~ 0.4 L_{MS} judged from its Raman spectra ($t_{\text{ox}} = 15$ s), $I_{\text{SHG}}^{\parallel}$ decreased by $\sim 75\%$ but still showed the same angular dependence as the pristine 1L_{MS}. The oxidation-induced modulation in I_{SHG} (Figs. 2a and 2b) and robust θ -dependence demonstrates the SHG process can be utilized in characterizing chemical changes in 2-dim materials.

Formation of ultraflat 2D oxides with a single-layer precision: The on-stack transformation was found to proceed in a layer-by-layer manner and could be controlled with a high thickness resolution even allowing formation of single-layer MoO₃. To monitor morphological changes by the transformation, an amplitude-modulated non-contact AFM was exploited. The height profile across the pristine 2L_{MS}-1L_{MS} area in Fig. 3a revealed a step with a height of 0.70 ± 0.1 nm, which agrees well with the interlayer spacing (0.62 nm) of 2H-MoS₂. [51] Note that the height of the 1L_{MS}-SiO₂ step varied in the range of $1.2 \sim 1.8$ nm from sample to sample due to the chemical and electrostatic contrast between dissimilar materials [52, 53] and interlayer molecular species trapped during the exfoliation. When 2L_{MS} was completely oxidized ($t_{\text{ox}} = 242$ s), the 2L_{MO}-1L_{MO} step height increased to 1.8 ± 0.1 nm (Fig. 3b & 3e). As depicted in Fig. 3f, the step height corresponds to the thickness of a single-layer MoO₃ and is ~ 2.5 times the interlayer spacing (0.69 nm) of α -MoO₃. [50] A similar change was observed for the 2L_{MS}-1L_{MS} step of another sample when treated for $t_{\text{ox}} = 242$ s (Fig. 3c & 3d). After the same treatment, however, the 3L_{MS}-2L_{MS} step height changed only by ~ 0.2 nm. In contrast to the 2L region, the Raman spectrum of the 3L region showed that $\sim 15\%$ of the lowermost layer still remained intact (see Fig. S5 for Raman spectra obtained after each step of

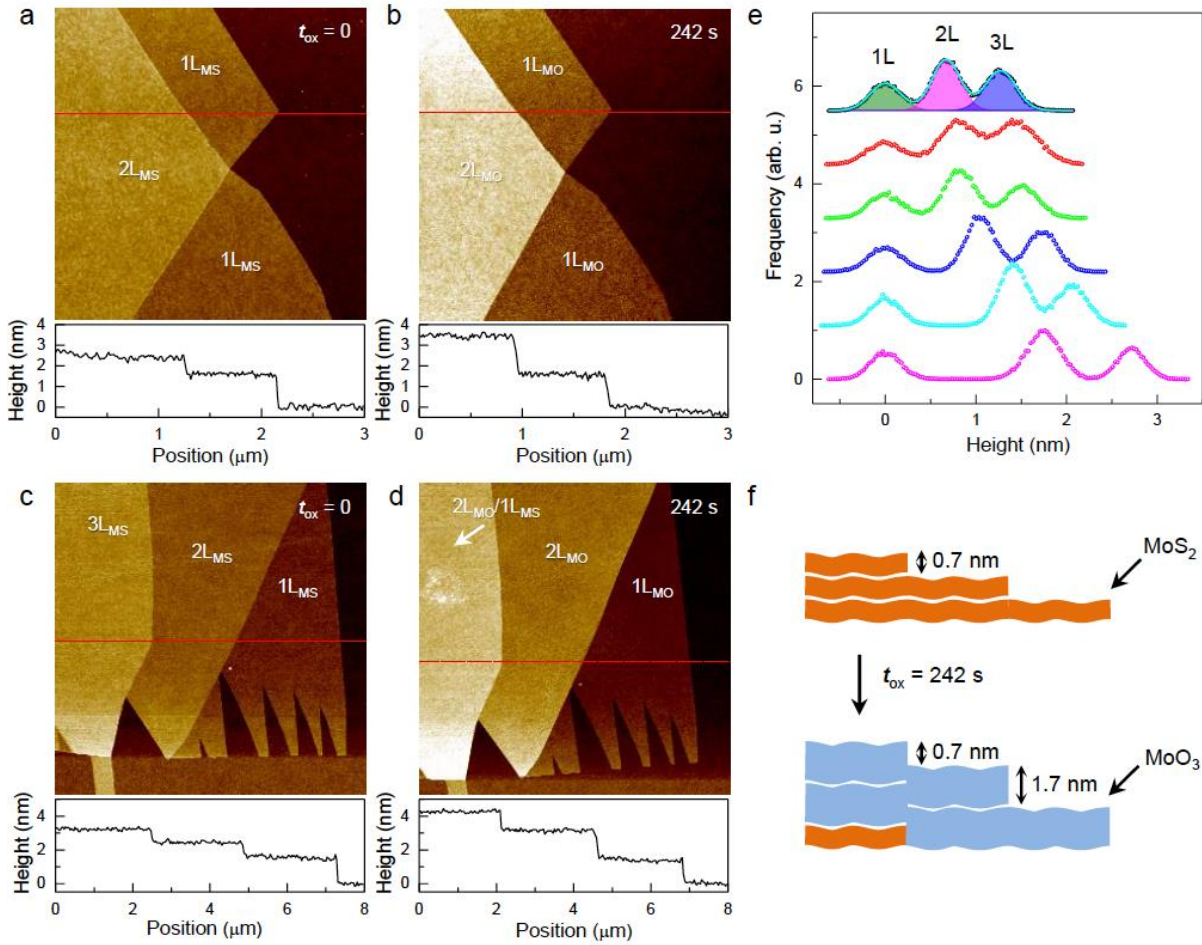


Figure 3. Layer-by-layer oxidation of few-layer MoS₂. (a) & (b) Non-contact AFM height images of a 1L_{MS}-2L_{MS} sample obtained before and after oxidation ($t_{\text{ox}} = 242$ s), respectively. Height profiles across the red lines in (a) and (b) are also shown below the AFM images. (c) & (d) Non-contact AFM height images of another sample with 1L_{MS}, 2L_{MS} and 3L_{MS} regions before and after oxidation ($t_{\text{ox}} = 242$ s), respectively. Height profiles across the red lines in (c) and (d) are also shown below the AFM images. (e) Height histograms of the sample in (c & d) obtained for the 1L, 2L and 3L areas as a function of t_{ox} (top to bottom): 0, 2, 8, 26, 80 & 242 s. The mean height of 1L area was set to be zero. Root-mean-square roughness (R_q) of each area was determined by fitting the data with 3 color-shaded Gaussian functions as shown for the pristine sample (see Fig. S6 for the variation of the roughness induced by the oxidation). (f) Schematic diagram of “top-down” layer-by-layer oxidation that converts MoS₂ into MoO₃.

the sequential oxidations). Thus, the step height measured across the 3L-2L region corresponds to the thickness of the partially oxidized bottom layer.

Despite the increase in the thickness, MoO₃ layers were still highly flat as can be seen in the AFM height images in Fig. 3. The change in the surface morphology of the 2D oxides was further quantified by the root-mean-square roughness (R_q) or standard deviation of height distribution shown in Fig. 3e. R_q of 1L_{MS}, 170 ± 10 pm which is slightly higher than that of graphene,[54] is equivalent to that of completely oxidized 1L_{MO}, 180 ± 10 pm for $t_{\text{ox}} \geq$

80 s as shown in Fig. S6. Notably, however, the surface roughness showed a spike of 230 ± 10 nm for $t_{\text{ox}} = 2$ s and a sharp decrease for $t_{\text{ox}} = 8$ s. Similar spikes were also observed for $2L_{\text{MS}}$ and $3L_{\text{MS}}$ when treated for 2 s. R_q 's of $2L_{\text{MO}}$ and $3L_{\text{MO}}$ (170 ± 10 nm) are also equivalent to those of their pristine counterparts. We attribute the roughness surge to clusters of partially oxidized MoS_2 , possibly molybdenum oxysulphides (MoS_xO_y)[55] which serve as nucleation sites during the plasma oxidation. This picture is also corroborated by the drastic PL quenching for $t_{\text{ox}} = 2$ s as will be shown below. However, the Raman spectra did not show a noticeable change (Fig. 1c & 1d) since majority of the sample remained intact for the short reaction time.

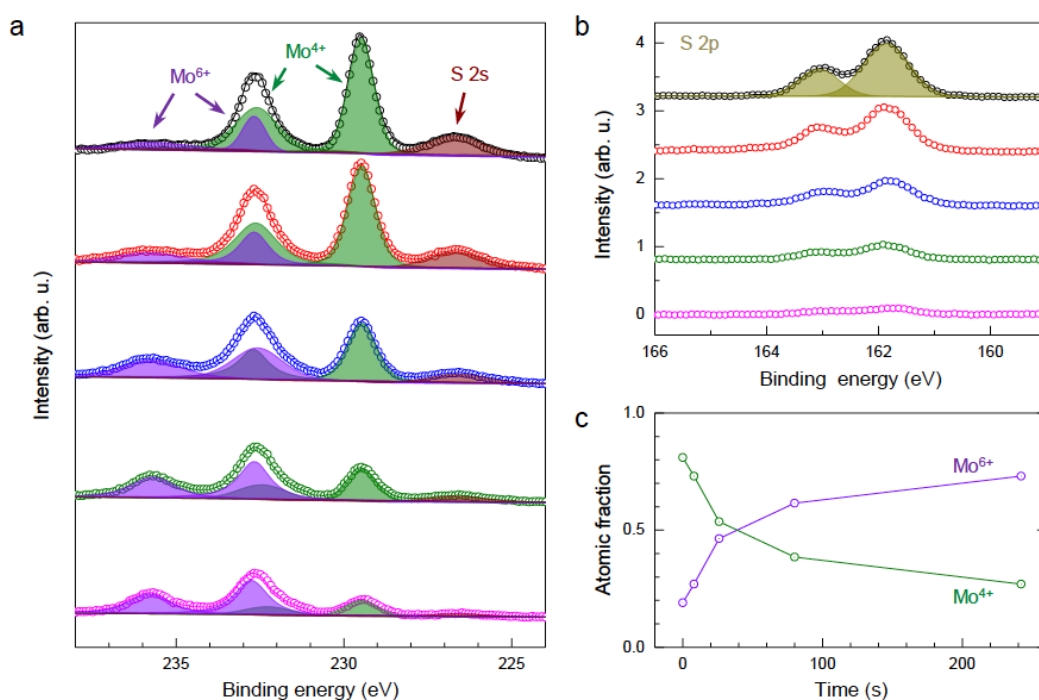


Figure 4. Elemental analysis of plasma-oxidized MoS_2 . (a) Mo 3d XPS spectra of CVD-grown $2L_{\text{MS}}$ samples oxidized for various t_{ox} (top to bottom): 0, 2, 8, 26, 80 & 242 s. The spectra were fitted with multiple mixed Lorentzian-Gaussian functions. The green shades correspond to Mo^{4+} ($3d_{5/2}$) and Mo^{4+} ($3d_{3/2}$) peaks, and the violet shades to Mo^{6+} ($3d_{5/2}$) and Mo^{6+} ($3d_{3/2}$) peaks. At the binding energy of ~ 227 eV, S 2s peak can be observed. (b) S 2p XPS spectra of the same samples shown in (a). The spectra were also fitted with two sub-peaks, $2p_{1/2}$ and $2p_{3/2}$. (c) The overall photoelectron intensity of Mo species and atomic fractions of Mo^{4+} and Mo^{6+} given as a function of t_{ox} .

Chemical nature of 2D oxides: The chemical transformation was revealed by the X-ray photoelectron spectroscopy (XPS). Because the probe size of the exploited XPS instrument was larger than the typical size (< 20 μm) of exfoliated samples, large-area MoS_2 films grown by the chemical vapor deposition (CVD) were exploited (see Methods for the details of preparation). Whereas the effective thickness was found to be 2L based on the peak difference ($\Delta\omega$), their Raman intensity was lower than that of mechanically exfoliated samples, suggesting lower

crystallinity (Fig. S7). Figure 4a presents the Mo 3d spectra obtained as a function of t_{ox} . The pristine sample showed the strong doublet of Mo^{4+} arising from MoS_2 with a binding energy (E_B) of 229.5 eV (232.6 eV) for $3d_{5/2}$ ($3d_{3/2}$), which is consistent with the average literature value of $E_B(3d_{5/2}) = 229.25$ eV for bulk MoS_2 crystals.[56] The Mo^{6+} species of the pristine sample, responsible for the minor doublet with $E_B = 232.7$ eV (235.7 eV) for $3d_{5/2}$ ($3d_{3/2}$), were attributed to residual MoO_3 (< 20% of the total Mo species) formed before or after the CVD growth. Upon the plasma treatment, the Mo^{6+} doublet significantly grew at the expense of the Mo^{4+} doublet indicating the conversion to MoO_3 . The oxidation was also confirmed by the decrease in the intensities of the S 2s peak ($E_B = 226.7$ eV) in Fig. 4a and S 2p doublet ($E_B = 161.9$ eV for $2p_{3/2}$) in Fig. 4b. The current data cannot exclude the possibility that a small fraction of Mo^{5+} species ($E_B = 231.1$ eV for $3d_{5/2}$)[57] representing oxygen vacancy defects generated by incomplete oxidation may be present.

To shed more light on the chemical transformation, we obtained optical absorption spectra using the reflectance spectroscopy in Fig. 5 (see Methods for the details). For a very thin film (thickness $\ll \lambda$) supported on a thick

transparent substrate with refractive index of n_0 , the fractional change in reflectance (δ_R) is given as follows: $\delta_R = \frac{R-R_0}{R_0} = \frac{4}{n_0^2-1}A$, where R , R_0 and A are reflectance of the film, reflectance of the bare substrate, and absorbance.[58] Pristine $1L_{\text{MS}} \sim 3L_{\text{MS}}$ exfoliated on quartz substrates showed characteristic absorption peaks at 1.90, 2.05 and 2.85 eV, which were denoted respectively by A, B and C according to an early work.[59] The two former excitonic peaks originate from the direct-gap transitions between the valence and conduction bands at the K points in the Brillouin zone.[5] The high energy peak, C, arises from nearly degenerate multiple excitonic states[60] or transitions across nested valence and conduction bands.[61] All the three peaks downshifted in energy with increasing thickness.[5] When the samples were treated for $t_{\text{ox}} = 80$ s which is expected to oxidize $\sim 1.7L$, the overall absorbance decreased significantly for all the thicknesses. The A & B peaks of $1L$, in particular, almost disappeared with the major absorption edges relocated to > 2.7 eV, which agrees well with the fact that MoO_3 is a wide-bandgap semiconductor.[62] The partially

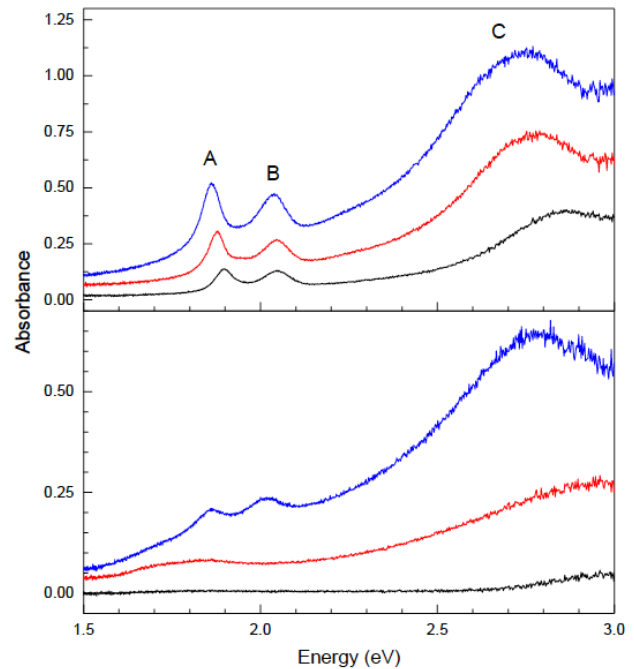


Figure 5. The absorption spectra of $1L \sim 3L$ MoS_2 exfoliated onto quartz substrates: (top) before and (bottom) after oxidation for $t_{\text{ox}} = 80$ s. The absorbance was determined from optical reflectance contrast measurements (see Methods for the details). See the text for the origins of the three prominent peaks denoted by A, B and C. For comparison with UV/Vis transmission measurements for CVD-grown samples and estimation of their optical bandgaps using Tauc plots, see Fig. S7.

oxidized 2L exhibited downshifts of A and B peaks but an upshift of C peak, the degree of which were much less for 3L. The spectral changes are attributed to the oxidation-induced defects and can be explained by the drastic changes in the electronic band structures of O-substituted MoS₂.^[63] To determine the optical bandgap of the 2D MoO₃, the Tauc plot analysis was taken for the UV/Vis absorption spectra of CVD-grown large-area samples (Fig. S8). Despite some inconsistencies in the literature,^[64] it is generally accepted that an optical gap energy (E_g) of an amorphous semiconductor can be extrapolated using $(\alpha h\nu)^{1/m} \propto (h\nu - E_g)$,^[65, 66] where α , $h\nu$ and m are respectively absorption coefficient, photon energy and exponent specifying the nature of the optical transition ($m = 2$ for an indirect allowed transition; $m = 1/2$ for a direct allowed transition). By choosing $m = 2$ for α -MoO₃ is an indirect bandgap semiconductor,^[67] E_g was determined to be ~ 3.0 eV for 1L_{MO} and 2L_{MO}. The resulting bandgap energies are in a good agreement with those of α -MoO₃ crystals^[62] and thermally deposited MoO₃ films.^[68, 69] Despite the similar bandgap energies and apparent layered structure of plasma-generated MoO₃, however, no Raman signal could be detected from the 2D oxides possibly due to their amorphous nature. A careful Raman analysis in comparison with mechanically exfoliated thin α -MoO₃ crystals set an upper bound for α -MoO₃ content $\sim 1\%$ (Fig. S9).

PL intensity modulation: The change in the photoluminescence (PL) spectra in Fig. 6 revealed further details of the chemical modifications occurring in MoS₂ thin membranes. The PL spectrum of the pristine 1L_{MS} mainly consists of the two exciton peaks, A and B, respectively located at 1.84 and 2.00 eV, which are in a good agreement with the absorption spectra. Both originate from the direct-gap transitions between the conduction and valence bands at the K points in the Brillouin zone.^[5, 7] First, we note that the PL is drastically quenched by the plasma treatments. After 2-s exposure, for example, the intensity of A (I_A) decreased by $\sim 65\%$ although the Raman spectra in Fig. 1 showed no significant change in $I(E_{2g}^1)$ and $I(A_{1g})$. The quenching can be attributed to the plasma-generated defects that were confirmed by the defect-induced Raman peaks, as will be further discussed below. When further defects were introduced to form the NC phase ($t_{ox} = 8$ s), the PL intensity was only $\sim 10\%$ of the pristine value. The completely oxidized 1L_{MO} gave no PL signal, which is consistent with the fact that its E_g is larger than the excitation photon energy of 2.41 eV. 2L_{MS} in Fig. 6b showed a similar defect-mediated PL quenching: $\sim 60\%$ decrease for $t_{ox} = 2$ s and almost zero PL signal for $t_{ox} = 8$ s which introduced significant amount of defects judged from the Raman spectrum (Fig. 1c). Upon further oxidation ($t_{ox} = 26$ s), however, the PL intensity increased back to $\sim 30\%$ of that for the pristine 2L_{MS}. We note that the Raman spectra showed that the top layer was almost completely oxidized with the bottom layer mostly intact (Fig. 1d). This suggests that the system essentially became a 1L_{MO}/1L_{MS}/SiO₂ sandwich, which further corroborates the layer-by-layer oxidation. Thicker samples showed a similar trend but the PL intensity oscillation of n L_{MS} could be seen only when t_{ox} was selected in such a way that $(n-1)$ L_{MO}/1L_{MS} was nicely formed.

Structural defects in crystalline semiconductors have various modes of interactions with excited charge carriers, and their interactions become more significant in lower dimensional materials due to confined wave functions within a tighter space. For carbon nanotubes with low lying dark exciton states, sp^3 -type defects form new sets of radiative energy levels endowing an enhanced PL quantum yield.[70] Defects may trap excited free charge carriers and mediate ultrafast Auger decay of photoexcitation in quantum dots.[71] Excitons can be localized at defects and radiatively decay at lower energies as shown for 1L MoS₂ irradiated with α particles[72] and 1L WS₂ treated with Ar plasma.[73] Defects in some 2D semiconductors were also shown to serve as single photon emitters.[74, 75] Localization followed by non-radiative decay is one among various quenching routes of excitons, which also include exciton-exciton annihilation and electron-phonon interactions.[76] The PL quenching observed at the very early stage of the oxidative conversion can be attributed to partially oxidized defects including the nanometer scale protrusions that were responsible for the roughness spikes (Fig. S6). The higher defect-sensitivity of PL can be more clearly seen in the comparison between Raman and PL intensities given as a function of t_{ox} (Fig. S10).

Layer-by-layer conversion: The overall change can be summarized by the scheme for 3L_{MS} with terraces of 2L_{MS} and 1L_{MS} presented in Fig. 3f. At the early stage of reactions ($t_{ox} = 2$ s), the top surface of 3L_{MS} exposed to the gaseous oxidants undergoes partial oxidation forming nanometer-scale oxysulfides (MoS_xO_y) clusters that are responsible for the increased R_q . At this stage, the average thickness of the top layer is not much different from that of pristine 1L_{MS} or the interlayer spacing of 2H-MoS₂ crystals. Although the Raman spectra reveal no significant change, the PL intensity of 3L_{MS} drops significantly due to the defects serving as PL quenchers. Additional exposure to oxidants induces the NC-phase Raman peaks and almost complete quenching of the PL. When the first top layer is completely converted to MoO₃, its thickness increases to 1.8 nm which is 2.5 times the interlayer spacing of α -MoO₃ crystals. At this stage where 1L_{MO}/2L_{MS} is formed, the PL intensity can be recovered back to that of 2L_{MS} because of lack of quenching sites within the remaining 2L_{MS}. Further exposure will repeat the above reactions for the second top layer but on a much decreased reaction rate.

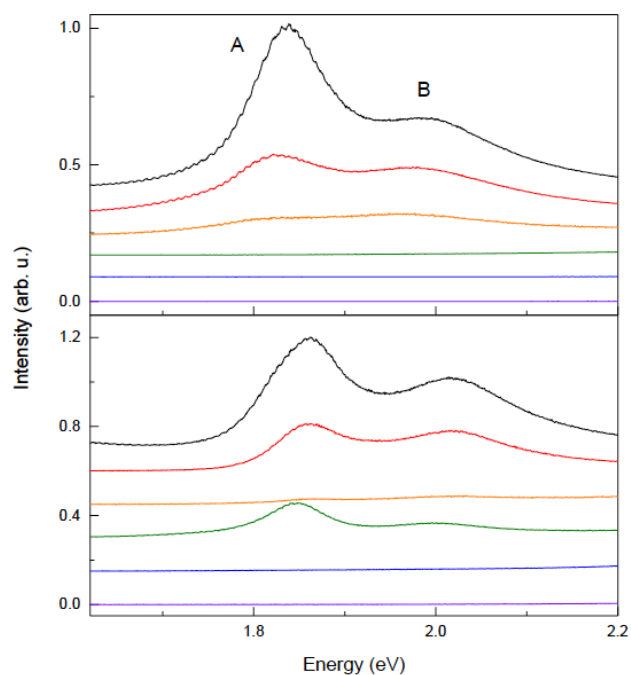


Figure 6. Photoluminescence spectra of 1L (top) and 2L (bottom) MoS₂ for varying t_{ox} (top to bottom): 0, 2, 8, 26, 80 & 242 s. The two emission peaks denoted by A and B have the same origins as the corresponding absorption peaks in Fig. 5.

Although the Raman analysis suggests that the 2D oxides are amorphous, their high flatness and modulation in SHG and PL intensities indicate that the oxidation reaction proceeds in the layer-by-layer manner. Thus, it is likely that the oxides are also layered like α -MoO₃. Since the number density of Mo in a single α -MoO₃ layer[67] is 18% higher than that for 1L_{MS},[51] a 2D conversion into the crystalline oxide would lead to a large tensile strain (~9%) when the areal density of Mo is maintained or generate voids requiring significant mass transport to compensate the difference in the Mo densities. Moreover, the average thickness of 1L_{MO} (Fig. 3) is 2.5 times the interlayer spacing of α -MoO₃. These facts suggest that the 2D oxides are much less dense than α -MoO₃. Despite the apparent flatness and lack of pits or cracks in the 2D oxides, these considerations lead us to a conclusion that there must be numerous structural irregularities including fine voids that cannot be detected by the AFM probes. Our results also showed that the plasma oxidation is highly effective for the topmost sulfide layer and increasingly slower for the next buried layers. Such voids may serve as a passage route for the oxidants required for the reactions underneath the top layer.

In summary, we demonstrated a model 2D chemical reaction that converts 1L sulfides into 1L oxides thus allowing MoO₃/MoS₂ heterostructure. Single and few-layer MoS₂ prepared via micromechanical exfoliation of 2H-MoS₂ crystals were treated with strong oxidants generated from O₂ plasma. The early stage of the reaction was detected by the defect-induced Raman peaks, drastic quenching of PL signals and sub-nm protrusions in AFM images. As the reaction proceeded from the uppermost layer to buried layers, PL and SHG signals showed characteristic modulations revealing a layer-by-layer conversion. The plasma-generated 2D oxides, confirmed as MoO₃ by XPS, were found to be amorphous but highly flat with a surface roughness of 0.18 nm, comparable to that of 1L MoS₂. The rate of oxidation quantified with Raman spectroscopy decreased very rapidly for buried sulfide layers due to protection by the surface 2D oxides. As exemplified in this work, the on-stack chemical transformation can be applied to other 2D materials in forming otherwise unobtainable materials and complex heterostructures, thus expanding the palette of 2D materials building blocks.

Experimental Section

Mechanical exfoliation. Single and few-layer MoS₂ samples were prepared by mechanical exfoliation[3] of molybdenite, a natural mineral of 2H-MoS₂ (SPI). Silicon wafers with 285-nm-thick SiO₂ layers were used as substrates. Ultrathin layers of MoS₂ were identified using an optical microscope and their numbers of layers and quality were determined using Raman spectroscopy.[6] To prepare thin α -MoO₃ crystalline flakes as a Raman standard (Fig. S9), a similar mechanical exfoliation was applied to a powder of MoO₃ (Materion).

Growth of large-area samples by CVD. Two different CVD growth methods were used in synthesizing large area MoS₂ films. In one approach for the samples used for XPS measurements, Mo metal of 0.5 nm for 2L_{MS} was deposited on SiO₂/Si substrates by e-beam evaporation. The samples were positioned in a quartz tube furnace, which was then evacuated to a low vacuum. The samples were heated to 750 °C under flow of Ar at a rate of 50 mL/min. Since the surface of deposited Mo films usually becomes oxidized when exposed to the ambient air during transfer to the furnace, a H₂ gas was briefly introduced at 750 °C to reduce the Mo oxides. After the pre-annealing and reduction processes, a H₂S/H₂/Ar gas mixture (1:5:50) was introduced for 15 min to sulfurize Mo films into MoS₂. The pressure in the furnace was maintained at 300 mTorr during the sulfurization step. To enhance the crystallinity of grown films, the samples were further annealed briefly at 1000 °C under a flow of H₂S/Ar gas mixture (1:50). In the other approach for the samples used UV/Vis measurements, 5 ~ 10 mg of MoO₃ powder (Sigma-Aldrich) in a quartz boat was placed at the center of the furnace and quartz substrates were placed near the boat in the downstream. The furnace was heated up to 600 °C at a rate of 20 °C/min under an Ar gas with a flow rate of 200 mL/min. At 600 °C, a H₂S gas was introduced at a rate of 1 mL/min to sulfurize MoO₃ into MoS₂ for 30 min. Then the samples were rapidly cooled down to room temperature. The average thickness and quality of grown films were characterized by their Raman and PL spectra.

Plasma oxidation. For oxidation, samples were treated with either of the two low-frequency plasma instruments operated at 50 kHz, a commercial unit (Femto Science Inc., Cute-1MP) and a quartz-tube-type unit. The partial pressure of O₂ in the two plasma chambers was 540 and 300 mTorr, respectively. For oxidation reactions, oxygen plasma was maintained for a pre-specified period of t_{ox} at a power of 10 W. Because of the differences in the instruments and detailed procedures, the apparent oxidation rate was ~3 times larger for the former than the latter. Thus, t_{ox} given in this work has been corrected for the difference.

Raman and PL Measurements. The Raman and PL spectra of the samples were obtained with a microscope-based (Nikon, Ti) Raman setup that is equivalent to what detailed elsewhere.[77, 78] Briefly, the 514 nm excitation beam from a solid state laser (Cobolt, Fangdango) was focused onto a spot of ~1 μm in diameter using an objective lens (40X, numerical aperture = 0.60). The back-scattered signal was collected by the same objective and guided to a spectrograph (Princeton Instruments, SP2300) combined with a liquid nitrogen-cooled charge-coupled detector (CCD) (Princeton Instruments, PyLon). The spectral resolution judged from the FWHM of the Rayleigh line was 3.0 and 12 cm⁻¹ for Raman and PL spectra, respectively.

SHG measurements. A similar microscope-based spectroscopy setup was employed for the SHG detection. A train of 140-fs pulses from a Ti:Sapphire laser (Coherent, Chameleon) operated at 800 nm was focused onto a spot of 1.6 μm in FWHM with an objective lens (40X, numerical aperture = 0.60). The backscattered SHG signal centered at 400 nm was collected and fed to a spectrograph (Andor, Shamrock 303i) equipped with a thermoelectrically

cooled CCD (Andor, Newton). To vary the polarization angle of the fundamental laser with respect to the MoS₂ lattice vectors, samples were rotated in a rotational mount with an angular accuracy better than 0.2 degree. For a polarized detection, the SHG signal was filtered with a polarizer located in front of the spectrograph.

AFM measurements. The topographic details of the samples were investigated by using an atomic force microscope (Park Systems, XE-70). The height images were obtained in a non-contact mode using Si tips with a nominal tip radius of 8 nm (MicroMasch, NSC-15). The AFM tip was driven to a free oscillation with an amplitude of 20 nm and engaged in amplitude-modulated scanning with an amplitude set-point of ~14 nm.

XPS measurements. The elemental information of the CVD-grown samples was obtained by using an X-ray photoelectron spectrometer (Thermo Scientific, K-Alpha^{TM+}). XPS measurements were carried out with Al K_α line (1.4866 keV). The binding energy of the photoelectrons was calibrated with respect to Mo(IV) 3d_{5/2} ($E_B = 229.5$ eV) which was more reliable than C 1s peak ($E_B = 284.6$ eV) originating from carbon residues on the samples.

Optical absorption measurements. For the samples exfoliated onto quartz substrates, the fractional changes in reflectance were used to obtain absorption spectra. As a broadband Vis/NIR light source, the output of a tungsten-halogen lamp (iiSM Inc., Mighty Light Beam) was collected with a multimode optical fiber (core diameter of 50 μm) and guided to the micro-spectroscopy setup exploited for the SHG measurements. The FWHM of the focus spot was 0.8 and 2.0 μm in the visible and NIR ranges, respectively. For the samples CVD-grown on quartz substrates, the absorption spectra were obtained with a UV/visible spectrometer (Jasco, V-650).

TEM measurements. For TEM measurements, MoS₂ flakes exfoliated onto SiO₂/Si substrates were transferred to carbon-film grids with 2-μm holes (Quantifoil) using isopropyl alcohol and KOH solution.[79] The samples were analyzed using an aberration-corrected FEI Titan Cubed TEM (FEI, Titan³ G2 60-300), which was operated at 80 kV acceleration voltage with a monochromator. The microscope provides sub-angstrom resolution at 80 kV and -11 ± 0.5 μm of spherical aberration (C_s).

ASSOCIATED CONTENT

Supporting Information. A. Optical contrast of plasma-oxidized MoS₂; B. Defect-activated scattering of LA(M) in plasma-oxidized MoS₂; C. TEM characterization of freestanding 1L MoS₂; D. Power dependence of SHG signal from 1L MoS₂; E. Thickness-dependent Raman characterization of plasma-oxidized MoS₂; F. Effect of O₂ plasma treatment on surface roughness of MoS₂; G. Comparison of CVD-grown and exfoliated MoS₂ using Raman spectroscopy; H. Optical bandgap of plasma-generated MoO₃; I. Possible content of α-MoO₃ in plasma-generated oxides; J. Oxidation-induced decays in Raman and PL signals of 1L ~ 4L MoS₂.

AUTHOR INFORMATION

Corresponding Author

*E-mail: sunryu@postech.ac.kr

ACKNOWLEDGMENT

This work was supported by the Center for Advanced Soft-Electronics funded by the Ministry of Science, ICT and Future Planning as Global Frontier Project (NRF-2014M3A6A5060934) and also by the National Research Foundation of Korea (NRF-2015R1A2A1A15052078).

REFERENCES

- [1] Novoselov K S, Geim A K, Morozov S V, Jiang D, Zhang Y, Dubonos S V, Grigorieva I V and Firsov A A 2004 Electric field effect in atomically thin carbon films *Science* **306** 666-669
- [2] Geim A K and Novoselov K S 2007 The rise of graphene *Nat. Mater.* **6** 183-191
- [3] Novoselov K S, Jiang D, Schedin F, Booth T J, Khotkevich V V, Morozov S V and Geim A K 2005 Two-dimensional atomic crystals *Proc. Natl. Acad. Sci. U. S. A.* **102** 10451-10453
- [4] Gorbachev R V, et al. 2011 Hunting for Monolayer Boron Nitride: Optical and Raman Signatures *Small* **7** 465-468
- [5] Mak K F, Lee C, Hone J, Shan J and Heinz T F 2010 Atomically Thin MoS₂: A New Direct-Gap Semiconductor *Phys. Rev. Lett.* **105** 136805
- [6] Lee C, Yan H, Brus L E, Heinz T F, Hone J and Ryu S 2010 Anomalous Lattice Vibrations of Single- and Few-Layer MoS₂ *ACS Nano* **4** 2695-2700
- [7] Splendiani A, Sun L, Zhang Y B, Li T S, Kim J, Chim C Y, Galli G and Wang F 2010 Emerging Photoluminescence in Monolayer MoS₂ *Nano Lett.* **10** 1271-1275
- [8] Radisavljevic B, Radenovic A, Brivio J, Giacometti V and Kis A 2011 Single-layer MoS₂ transistors *Nat. Nanotechnol.* **6** 147-150
- [9] Britnell L, et al. 2012 Electron Tunneling through Ultrathin Boron Nitride Crystalline Barriers *Nano Lett.* **12** 1707-1710
- [10] Stolyarova E, Rim K T, Ryu S, Maultzsch J, Kim P, Brus L E, Heinz T F, Hybertsen M S and Flynn G W 2007 High-resolution scanning tunneling microscopy imaging of mesoscopic graphene sheets on an insulating surface *Proc. Natl. Acad. Sci. U. S. A.* **104** 9209-9212
- [11] Ishigami M, Chen J H, Cullen W G, Fuhrer M S and Williams E D 2007 Atomic Structure of Graphene on SiO₂ *Nano Lett.* **7** 1643-1648
- [12] Ataca C, Sahin H and Ciraci S 2012 Stable, Single-Layer MX₂ Transition-Metal Oxides and Dichalcogenides in a Honeycomb-Like Structure *J. Phys. Chem. C* **116** 8983-8999
- [13] Kim K S, Zhao Y, Jang H, Lee S Y, Kim J M, Kim K S, Ahn J-H, Kim P, Choi J-Y and Hong B H 2009 Large-scale pattern growth of graphene films for stretchable transparent electrodes *Nature* **457** 706-710
- [14] Li X S, et al. 2009 Large-Area Synthesis of High-Quality and Uniform Graphene Films on Copper Foils *Science* **324** 1312-1314

- [15] Shi Y M, et al. 2012 van der Waals Epitaxy of MoS₂ Layers Using Graphene As Growth Templates *Nano Lett.* **12** 2784-2791
- [16] Zhan Y, Liu Z, Najmaei S, Ajayan P M and Lou J 2012 Large-Area Vapor-Phase Growth and Characterization of MoS₂ Atomic Layers on a SiO₂ Substrate *Small* **8** 966-971
- [17] Kim K K, et al. 2012 Synthesis of Monolayer Hexagonal Boron Nitride on Cu Foil Using Chemical Vapor Deposition *Nano Lett.* **12** 161-166
- [18] Novoselov K S and Castro Neto A H 2012 Two-dimensional crystals-based heterostructures: materials with tailored properties *Phys. Scr.* **T146** 014006
- [19] Ponomarenko L A, et al. 2011 Tunable metal-insulator transition in double-layer graphene heterostructures *Nat. Phys.* **7** 958-961
- [20] Britnell L, et al. 2012 Field-Effect Tunneling Transistor Based on Vertical Graphene Heterostructures *Science* **335** 947-950
- [21] Britnell L, et al. 2013 Strong Light-Matter Interactions in Heterostructures of Atomically Thin Films *Science* **340** 1311-1314
- [22] Liu H, Ryu S, Chen Z, Steigerwald M L, Nuckolls C and Brus L E 2009 Photochemical Reactivity of Graphene *J. Am. Chem. Soc.* **131** 17099-17101
- [23] Liu L, Ryu S, Tomasik M R, Stolyarova E, Jung N, Hybertsen M S, Steigerwald M L, Brus L E and Flynn G W 2008 Graphene Oxidation: Thickness Dependent Etching and Strong Chemical Doping *Nano Lett.* **8** 1965-1970
- [24] Sharma R, Baik J H, Perera C J and Strano M S 2010 Anomalously Large Reactivity of Single Graphene Layers and Edges toward Electron Transfer Chemistries *Nano Lett.* **10** 398-405
- [25] Yamamoto M, Einstein T L, Fuhrer M S and Cullen W G 2012 Charge Inhomogeneity Determines Oxidative Reactivity of Graphene on Substrates *ACS Nano* **6** 8335-8341
- [26] Nakada K, Fujita M, Dresselhaus G and Dresselhaus M S 1996 Edge state in graphene ribbons: nanometer size effect and edge shape dependence *Phys. Rev. B: Condens. Matter* **54** 17954-17961
- [27] Cullen W G, Yamamoto M, Burson K M, Chen J H, Jang C, Li L, Fuhrer M S and Williams E D 2010 High-Fidelity Conformation of Graphene to SiO₂ Topographic Features *Phys. Rev. Lett.* **105** 215504
- [28] Sutter P, Hybertsen M S, Sadowski J T and Sutter E 2009 Electronic Structure of Few-Layer Epitaxial Graphene on Ru(0001) *Nano Lett.* **9** 2654-2660
- [29] Rafiee J, Mi X, Gullapalli H, Thomas A V, Yavari F, Shi Y F, Ajayan P M and Koratkar N A 2012 Wetting transparency of graphene *Nat. Mater.* **11** 217-222
- [30] Jaegermann W and Schmeisser D 1986 Reactivity of layer type transition metal chalcogenides towards oxidation *Surf. Sci.* **165** 143-160
- [31] Lin Y C, Zhang W J, Huang J K, Liu K K, Lee Y H, Liang C T, Chu C W and Li L J 2012 Wafer-scale MoS₂ thin layers prepared by MoO₃ sulfurization *Nanoscale* **4** 6637-6641
- [32] Lu X, et al. 2014 Large-Area Synthesis of Monolayer and Few-Layer MoSe₂ Films on SiO₂ Substrates *Nano Lett.* **14** 2419-2425
- [33] Xu X, Yao W, Xiao D and Heinz T F 2014 Spin and pseudospins in layered transition metal dichalcogenides *Nat. Phys.* **10** 343-350
- [34] Wang Q H, Kalantar-Zadeh K, Kis A, Coleman J N and Strano M S 2012 Electronics and optoelectronics of two-dimensional transition metal dichalcogenides *Nat. Nanotechnol.* **7** 699-712
- [35] Yao J N, Hashimoto K and Fujishima A 1992 Photochromism induced in an electrolytically pretreated MoO₃ thin film by visible light *Nature* **355** 624
- [36] Yao J N, Yang Y A and Loo B H 1998 Enhancement of photochromism and electrochromism in MoO₃/Au and MoO₃/Pt thin films *J. Phys. Chem. B* **102** 1856-1860
- [37] Gesheva K, Szekeres A and Ivanova T 2003 Optical properties of chemical vapor deposited thin films of molybdenum and tungsten based metal oxides *Sol. Energy Mater. Sol. Cells* **76** 563-576
- [38] Meyer J, Hamwi S, Kroeger M, Kowalsky W, Riedl T and Kahn A 2012 Transition Metal Oxides for Organic Electronics: Energetics, Device Physics and Applications *Adv. Mater.* **24** 5408-5427
- [39] Lembke D, Bertolazzi S and Kis A 2015 Single-Layer MoS₂ Electronics *Acc. Chem. Res.* **48** 100-110

- [40] Liu S W, Divayana Y, Sun X W, Wang Y, Leck K S and Demir H V 2011 Improved performance of organic light-emitting diodes with MoO₃ interlayer by oblique angle deposition *Opt. Express* **19** 4513-4520
- [41] Liu K-K, et al. 2012 Growth of Large-Area and Highly Crystalline MoS₂ Thin Layers on Insulating Substrates *Nano Lett.* **12** 1538-1544
- [42] Verble J L and Wieting T J 1970 Lattice mode degeneracy in MoS₂ and other layer compounds *Phys. Rev. Lett.* **25** 362-365
- [43] Zhao Y, et al. 2013 Inter layer Breathing and Shear Modes in Few-Trilayer MoS₂ and WSe₂ *Nano Lett.* **13** 1007-1015
- [44] Mignuzzi S, Pollard A J, Bonini N, Brennan B, Gilmore I S, Pimenta M A, Richards D and Roy D 2015 Effect of disorder on Raman scattering of single-layer MoS₂ *Phys. Rev. B* **91** 195411
- [45] Richter H, Wang Z P and Ley L 1981 THE ONE PHCNON RAMAN SPECTRUM IN MICROCRYSTALLINE SILICON *Solid State Commun.* **39** 625
- [46] Berkdemir A, et al. 2013 Identification of individual and few layers of WS₂ using Raman Spectroscopy *Sci. Rep.* **3** 1755
- [47] Shen Y R 1989 SURFACE-PROPERTIES PROBED BY 2ND-HARMONIC AND SUM-FREQUENCY GENERATION *Nature* **337** 519-525
- [48] Li Y, Rao Y, Mak K F, You Y, Wang S, Dean C R and Heinz T F 2013 Probing Symmetry Properties of Few-Layer MoS₂ and h-BN by Optical Second-Harmonic Generation *Nano Lett.* **13** 3329-3333
- [49] Ruppert C, Li Y, Wang L, Shih E-M, Hone J and Heinz T. In *Tunable optical second-harmonic generation from bilayer MoS₂ by controlled inversion symmetry breaking* APS March Meeting 2016 (<http://meetings.aps.org/link/BAPS.2016.MAR.Y17.5>), Baltimore, USA, Baltimore, USA, 2016
- [50] Andersson G and Magneli A 1950 On the Crystal Structure of Molybdenum Trioxide *Acta Chem. Scand.* **4** 793
- [51] Wakabayashi N, Smith H G and Nicklow R M 1975 Lattice dynamics of hexagonal MoS₂ studied by neutron scattering *Phys. Rev. B* **12** 659-663
- [52] Guggisberg M, Bammerlin M, Loppacher C, Pfeiffer O, Abdurixit A, Barwich V, Bennewitz R, Baratoff A, Meyer E and Guntherodt H J 2000 Separation of interactions by noncontact force microscopy *Phys. Rev. B* **61** 11151-11155
- [53] Shim J, Lui C H, Ko T Y, Yu Y-J, Kim P, Heinz T F and Ryu S 2012 Water-Gated Charge Doping of Graphene Induced by Mica Substrates *Nano Lett.* **12** 648-654
- [54] Hong J, Park M K, Lee E J, Lee D, Hwang D S and Ryu S 2013 Origin of New Broad Raman D and G Peaks in Annealed Graphene *Sci. Rep.* **3** 2700
- [55] Brown N M D, Cui N Y and Mckinley A 1998 An XPS study of the surface modification of natural MoS₂ following treatment in an RF-oxygen plasma *Appl. Surf. Sci.* **134** 11-21
- [56] Baker M A, Gilmore R, Lenardi C and Gissler W 1999 XPS investigation of preferential sputtering of S from MoS₂ and determination of MoS_x stoichiometry from Mo and S peak positions *Appl. Surf. Sci.* **150** 255-262
- [57] Deng X, Quek S Y, Biener M M, Biener J, Kang D H, Schalek R, Kaxiras E and Friend C M 2008 Selective thermal reduction of single-layer MoO₃ nanostructures on Au(111) *Surf. Sci.* **602** 1166-1174
- [58] Mak K F, Sfeir M Y, Wu Y, Lui C H, Misewich J A and Heinz T F 2008 Measurement of the Optical Conductivity of Graphene *Phys. Rev. Lett.* **101** 196405
- [59] Wilson J A and Yoffe A D 1969 The transition metal dichalcogenides discussion and interpretation of the observed optical, electrical and structural properties *Adv. Phys.* **18** 193
- [60] Qiu D Y, Da Jornada F H and Louie S G 2013 Optical Spectrum of MoS₂: Many-Body Effects and Diversity of Exciton States *Phys. Rev. Lett.* **111**
- [61] Carvalho A, Ribeiro R M and Castro Neto A H 2013 Band nesting and the optical response of two-dimensional semiconducting transition metal dichalcogenides *Phys. Rev. B* **88**
- [62] Juryska R 1975 Optical absorption and electronic transitions in MoO₃ single crystals *Phys. Status Solidi B* **72** K161
- [63] Kang N, Paudel H P, Leuenberger M N, Tetard L and Khondaker S I 2014 Photoluminescence Quenching in Single-Layer MoS₂ via Oxygen Plasma Treatment *J. Phys. Chem. C* **118** 21258-21263

- [64] Lopez R and Gomez R 2012 Band-gap energy estimation from diffuse reflectance measurements on sol-gel and commercial TiO₂: a comparative study *J. Sol-Gel Sci. Technol.* **61** 1-7
- [65] Tauc J, Grigorovici R and Vancu A 1966 Optical Properties and Electronic Structure of Amorphous Germanium *Phys. Status Solidi* **15** 627
- [66] Wood D L and Tauc J 1972 Weak Absorption Tails in Amorphous Semiconductors *Phys. Rev. B* **5** 3144
- [67] Scanlon D O, Watson G W, Payne D J, Atkinson G R, Egdell R G and Law D S L 2010 Theoretical and Experimental Study of the Electronic Structures of MoO₃ and MoO₂ *J. Phys. Chem. C* **114** 4636-4645
- [68] Sian T S and Reddy G B 2004 Optical, structural and photoelectron spectroscopic studies on amorphous and crystalline molybdenum oxide thin films *Sol. Energy Mater. Sol. Cells* **82** 375-386
- [69] Hussain Z 2001 Optical and electrochromic properties of heated and annealed MoO₃ thin films *J. Mater. Res.* **16** 2695-2708
- [70] Piao Y, Meany B, Powell L R, Valley N, Kwon H, Schatz G C and Wang Y 2013 Brightening of carbon nanotube photoluminescence through the incorporation of sp(3) defects *Nat. Chem.* **5** 840-845
- [71] Klimov V I, Mikhailovsky A A, McBranch D W, Leatherdale C A and Bawendi M G 2000 Quantization of multiparticle Auger rates in semiconductor quantum dots *Science* **287** 1011-1013
- [72] Tongay S, et al. 2013 Defects activated photoluminescence in two-dimensional semiconductors: interplay between bound, charged, and free excitons *Sci. Rep.* **3**
- [73] Chow P K, Jacobs-Gedrim R B, Gao J, Lu T M, Yu B, Terrones H and Koratkar N 2015 Defect-Induced Photoluminescence in Mono layer Semiconducting Transition Metal Dichalcogenides *ACS Nano* **9** 1520-1527
- [74] Koperski M, Nogajewski K, Arora A, Cherkez V, Mallet P, Veuillen J Y, Marcus J, Kossacki P and Potemski M 2015 Single photon emitters in exfoliated WSe₂ structures *Nat. Nanotechnol.* **10** 503-506
- [75] Srivastava A, Sidler M, Allain A V, Lembke D S, Kis A and Imamoglu A 2015 Optically active quantum dots in monolayer WSe₂ *Nat. Nanotechnol.* **10** 491-496
- [76] Harrah D M and Swan A K 2011 The Role of Length and Defects on Optical Quantum Efficiency and Exciton Decay Dynamics in Single-Walled Carbon Nanotubes *ACS Nano* **5** 647-655
- [77] Lee J E, Ahn G, Shim J, Lee Y S and Ryu S 2012 Optical separation of mechanical strain from charge doping in graphene *Nat. Commun.* **3** 1024
- [78] Lee D, Ahn G and Ryu S 2014 Two-Dimensional Water Diffusion at a Graphene-Silica Interface *J. Am. Chem. Soc.* **136** 6634-6642
- [79] Meyer J C, Girit C O, Crommie M F and Zettl A 2008 Hydrocarbon lithography on graphene membranes *Appl. Phys. Lett.* **92** 123110